Numerical study of liquid imbibition and contact line pinning in a sealing gap for corrosion protection of metal housings

Daniel Hagg*, Alexander Eifert and Torsten Troßmann

Robert Bosch GmbH,
Robert-Bosch-Campus 1,
71272 Renningen, Germany
Email: DanielMaximilian.Hagg@de.bosch.com
Email: Alexander.Eifert@de.bosch.com
Email: Torsten.Trossmann@de.bosch.com
*Corresponding author

Bettina Frohnapfel

Institute of Fluid Mechanics,
Karlsruhe Institute of Technology (KIT),
Kaiserstr. 10, 76131 Karlsruhe, Germany
Email: bettina.frohnapfel@kit.edu

Holger Marschall

Computational Multiphase Flow,
Technical University Darmstadt,
Alarich-Weiss-Straße 10,
64287 Darmstadt, Germany
Email: marschall@mma.tu-darmstadt.de

Martin Wörner

Institute of Catalysis Research and Technology,
Karlsruhe Institute of Technology (KIT),
Engesserstr. 20, 76131 Karlsruhe, Germany
Email: martin.woerner@kit.edu

Abstract: Sealing gaps are common in housings that protect sensitive assemblies from potential damage by the environment. A prevalent measure to prevent water from reaching the sealing ring are pinning grooves. In this work, the influence of material wettability on the capillary-driven penetration of water into a generalised sealing gap geometry with pinning groove is investigated numerically for the first time. Interface-resolving two-phase flow simulations are performed with a diffuse-interface phase-field method solving the coupled Cahn-Hilliard Navier-Stokes equations. In the simulations of a gap geometry with pinning groove, the imbibition process is slowed down but not stopped for contact angles up to about 50°, while imbibition is prevented for contact angles larger than about 55°. The different behaviour is explained by the edge effect in wetting which interacts with liquid inertia. Volume-of-fluid simulations performed for comparison show similar behaviour with slight differences in imbibition speed and much higher spurious currents.

Keywords: Cahn-Hilliard; capillarity; diffuse interface; edge effect in wetting; electronic housing; imbibition; phase-field method; sealing gap; two-phase simulation; volume-of-fluid; VOF.

Reference to this paper should be made as follows: Hagg, D., Eifert, A., Troßmann, T., Frohnapfel, B., Marschall, H. and Wörner, M. (2024) 'Numerical study of liquid imbibition and contact line pinning in a sealing gap for corrosion protection of metal housings', *Progress in Computational Fluid Dynamics*, Vol. 24, No. 2, pp.65–77.

Alexander Eifert received his PhD from the Technical University of Darmstadt, Germany in 2015. Currently, he is a research engineer at the Corporate Research Center of Robert Bosch GmbH. His research interests are fluid-surface interaction, wetting on surfaces, and computational fluid dynamics.

Torsten Troßmann received his PhD from the Technical University of Darmstadt, Germany in 2005. Currently, he is a Senior Manager at the Corporate Research of the Robert Bosch GmbH. His research interests are the virtualisation of surface interactions and corrosive degradation.

Bettina Frohnapfel is a Full Professor at the Karlsruhe Institute of Technology (KIT), Germany. She heads the Institute of Fluid Mechanics (ISTM) at KIT.

Holger Marschall studied Chemical Engineering at the Technical University of Munich (TUM), Germany. He graduated as an Engineer (Dipl-Ing) in 2006 and received his PhD in 2011 at the same university. He is currently the Head of the Research Group Computational Multiphase Flow at Technical University of Darmstadt, Germany. He is seeking to understand fundamental properties of complex multiphase systems. For this, he develops high-fidelity simulation methods using the open-source C++ library OpenFOAM for computational continuum physics and multi-physics.

Martin Wörner studied Mechanical Engineering at the University of Karlsruhe (TH), Germany. After graduating as an Engineer (Dipl-Ing) in 1989, he received his doctoral degree (Dr-Ing) in 1994 at the same faculty. Throughout his professional career, he has worked at various institutes of today's Karlsruhe Institute of Technology (KIT) and its predecessor institutions, the Nuclear Research Center Karlsruhe and the Research Center Karlsruhe. His current position is the Head of the Multiphase Flow Group at the Institute of Catalysis Research and Technology (IKFT) at KIT. His scientific interests are the development of methods and computer codes for numerical simulation of multi-phase flows and their utilisation to study fundamental and technical aspects of two-phase flows in mechanical engineering and process engineering. Since 2003, he lectures on numerical modelling of multiphase flows at KIT.

1 Introduction

Static seals that protect critical parts from environmental influences are present in countless engineering applications from hydraulic systems to electronic housings. In Figure 1, a common sealing gap is shown schematically. In order to ensure the reliability of the sealing, various tests have to be conducted that fit the corresponding application. For instance, such tests concern the influence of different media, corrosive additives or the impact of pressure. The efficiency and durability of the sealing depends, among other things, on the sealing gap that protects the sealing ring (O-ring) from direct environmental influences. A pinning groove (cf. Figure 1) may stop liquid penetration ahead of the sealing ring to mitigate corrosion damage of the elastomer or rubber material (Zeng et al., 2021). The physical principle behind the groove is the pinning of the advancing contact line at the edge of the groove causing ultimately a situation with a static meniscus.

Inhibition of the liquid spreading by a sharp edge (edge effect) was proposed by Gibbs (1961), see also Dyson (1988). In Figure 2, the edge effect is graphically illustrated for liquid spreading on top of a solid surface (Oliver et al., 1977; Grishaev et al., 2013). According to the Gibbs criterion there exists a certain range for the apparent contact angle (θ) where the contact line is pinned at a solid edge with opening angle $\pi - \alpha$. For a material with equilibrium contact θ_e, this range is given by $\theta_e \leq \theta \leq \theta_{\text{cr}}$, where the upper critical value is $\theta_{\text{cr}} = \theta_e + \alpha$. An example for the utilisation of meniscus pinning at sharp edges of sudden channel enlargements are microfluidic capillary stop valves (Zimmermann et al., 2008). Pinning can also occur on seemingly flat substrates for example due to surface roughness which has an equivalent effect as pinning edges but on a smaller scale.

Figure 1 Sketch of a water droplet penetrating into a sealing gap protecting an electronic component (see online version for colours)

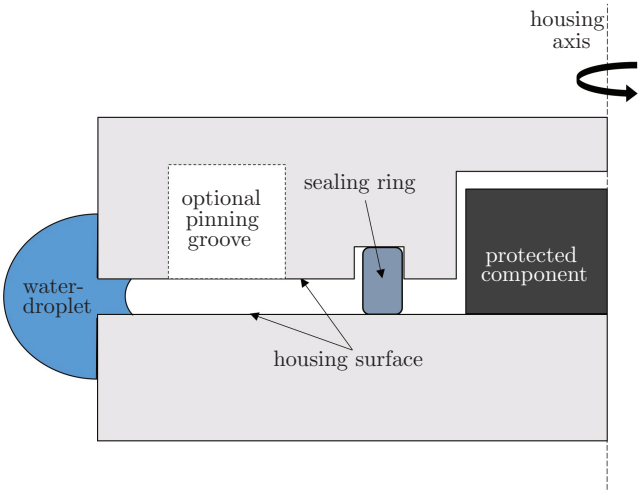

The geometry of sealing gaps with a pinning groove is mostly designed based on experience and experimental validation. The experimental validation takes time and sample parts have to be manufactured. This makes larger test series with geometric modifications and multiple iterations impractical. As a potentially fast and efficient alternative for evaluating different geometries and use cases, computational fluid dynamic is of high relevance to optimise the design of sealing gap geometries with pinning grooves. Previous numerical studies that considered capillary driven liquid penetration into more complex geometries used the level-set method (Gosselin et al., 2015), the Lattice-Boltzmann method (Wiklund, 2012) and the phase-field method (Mehrabian et al., 2011; Xiao et al., 2019). An overview over recent developments in interface-capturing methods for two-phase flows is given by Mirjalili et al. (2017).

Figure 2 Schematic illustration to explain the pinning at an ideal acute solid edge with opening angle $\pi - \alpha$ (see online version for colours)

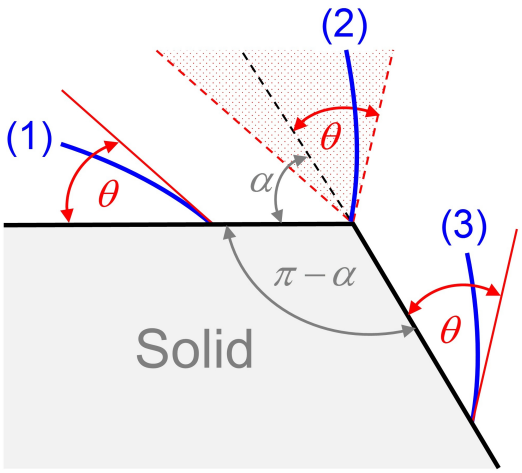

Notes: A liquid front (blue line) approaches the edge with contact angle θ (1); the liquid does not move over the edge until the apparent contact angle becomes $\alpha + \theta$ (2) and finally moves over when the angle exceeds $\alpha + \theta$ (3). In the pinned state, the slope of the liquid-gas interface lies in the dotted sector.

Source: Adapted from Grishaev et al. (2013)

For interface-capturing numerical simulation of two-phase flows, the volume-of-fluid (VOF) method is often considered as standard, either in its algebraic or geometrical version (Wörner, 2012). For capillary and wetting two-phase flows, however, several studies report severe shortcomings of the VOF method. Errors mainly originate from unphysical spurious currents caused by inaccurate calculation of the surface tension force, that plays a dominant role in capillary driven imbibition. In a comparison between different methods and solvers for transient capillary rise, the VOF method showed the largest errors due to spurious currents (Gründing et al., 2020). Furthermore, the algebraic VOF method in the standard OpenFOAM VOF solver `interFoam` has been shown to be unsuitable for droplet spreading simulations with a dynamic contact angle model due to the high spurious currents at the contact line (Antritter et al., 2020). An alternative method that is well suited for the simulation of capillary and wetting flows is the phase-field method (Jacqmin, 1999). The phase-field method is a diffuse interface method that allows for diffusive motion of the three-phase contact line in combination with the usual no-slip condition for the velocity field at solid walls. He and Kasagi (2008) compared a continuous-surface-force (CSF) model with a chemical potential model in a phase-field method, where the chemical potential model showed significantly lower spurious currents. Lee et al. (2020) proposed a boundary condition that pins the three-phase contact line on a flat surface using the Allen-Cahn version of the phase-field method. Peng et al. (2021) used the phase-field method to investigate imbibition in a straight microcapillary for liquid-liquid systems and provided a detailed study on the effects of different numerical parameters.

In this work, we present to the best of our knowledge the first numerical simulations of the influence of the material contact angle on the capillary-driven penetration of water into a complex sealing gap geometry with a pinning groove. To allow for a systematic investigation on the influence of wettability, the study is restricted to 2D planar configurations in order to limit the computational costs. The majority of the numerical simulations are performed with a phase field method implemented in OpenFOAM (FOAM-extend, solver `phaseFieldFoam`). The code has been carefully validated against various experiments on droplet spreading dynamics (Fink et al., 2018; Börnhorst et al., 2019; Samkhaniani et al., 2021; Wörner et al., 2021) and shows significantly lower spurious currents as compared to `interFoam` (Jamshidi et al., 2019). For comparison, two cases are simulated with the latter VOF solver as well. The influence of the wettability of the housing material is studied for different values of the contact angle without applying any special pinning boundary condition. The numerical results confirm the critical role of the edge effect to prevent water from entering the sealing gap. Although the present study is restricted to 2D simulations, the results suggest that the phase-field method is well suited for engineering computations of liquid imbibition with potential contact line pinning in 3D technical geometries.

In Section 2, the phase-field method and the solvers `phaseFieldFoam` and `interFoam` are briefly introduced. In the diffuse-interface approach the speed of the three-phase contact line depends on the mobility (M), which is a diffusion parameter that needs to be determined empirically. In Section 3, appropriate values for M are identified by comparing numerical results for the capillary rise in a planar gap with classical approximate solutions for two different values of the equilibrium contact angle. In Section 4, the water penetration into the complex geometry of a planar sealing gap with pinning groove is studied for solid materials with six different contact angles ranging from good ($\theta_e = 40°$) to reduced wettability ($\theta_e = 85°$).

2 Governing equations and numerical method

2.1 Phase-field method

The phase-field method considers the interfaces being diffuse and thereby follows ideas first proposed by van der Waals (1893). It is based on the variational minimisation of the Helmholtz free energy as described by Cahn and Hilliard (1958). Here, phases are distinguished by an order parameter (c) which takes the value of $c = -1$ in the gas phase and $c = 1$ in the liquid phase.

The total Helmholtz free energy (F) is composed of the mixture energy term and an additional term at solid boundaries, i.e., $F = F_{\text{mix}} + F_{\text{wall}}$. The mixture energy is given by

$$F_{\text{mix}}(c, |\nabla c|) = \int_V \left[\frac{\lambda}{\varepsilon^2} \Psi(c) + \frac{\lambda}{2} |\nabla c|^2 \right] \mathrm{d}V. \tag{1}$$

Here, the first part of F_{mix} describes the bulk energy of the system whereas the second term describes the gradient energy, which represents the interfacial energy density. In equation (1), λ is the mixing energy density and ε the capillary width that determines the thickness of the diffuse interface. The function Ψ is a double-well potential with two minima ($\Psi = 0$) corresponding to the pure gas and liquid phases chosen here as (Ginzburg and Landau, 1950)

$$\Psi(c) = \frac{1}{4}(c+1)^2(c-1)^2 = \frac{1}{4}(c^2-1)^2. \tag{2}$$

The chemical potential (ϕ_{mix}) is defined as the variational derivative of F_{mix} given by

$$\phi_{\text{mix}} := \frac{\delta F_{\text{mix}}}{\delta c} = \frac{\lambda}{\varepsilon^2}(c^3 - c) - \lambda \nabla^2 c. \tag{3}$$

If the chemical potential is uniformly zero, an equilibrium state is reached for the order parameter. The solution of equation (3) is then, assuming a planar interface, given by

$$c_e(x) = \tanh\left(\frac{n}{\sqrt{2}\varepsilon} \right), \tag{4}$$

where n denotes the coordinate normal to the interface (located at $c = 0$). This equilibrium profile leads to a thickness L_{di} of the diffuse interface over the range $-0.9 \leq c \leq 0.9$ of $L_{\text{di}} \approx 4\varepsilon$. The bulk potential integrated normal to the interface equals the interfacial tension, which is given by (Bray, 1994):

$$\sigma = \int_{-\infty}^{\infty} \lambda \left(\frac{\mathrm{d}c}{\mathrm{d}n} \right)^2 \mathrm{d}n = \frac{2\sqrt{2}}{3} \frac{\lambda}{\varepsilon}. \tag{5}$$

The latter relation is used to determine λ from given values of σ and ε.

The second term contributing to the free energy is given by (Jacqmin, 2000; Yue et al., 2010)

$$F_{\text{wall}}(c) = \int_A \left[-\frac{\sigma}{4}(3c - c^3)\cos\theta_e + \frac{\sigma_{ls} + \sigma_{gs}}{2} \right] \mathrm{d}A. \tag{6}$$

Here, θ_e is the equilibrium contact angle on a smooth surface while σ_{ls} and σ_{gs} denote the surface energies between liquid-solid and gas-solid, respectively. The wall chemical potential is defined as the variational derivative of F_{wall}, viz.

$$\phi_{\text{wall}} := \frac{\delta F_{\text{wall}}}{\delta c} = \frac{3}{4}\sigma(1 - c^2)\cos\theta_e. \tag{7}$$

Assuming an equilibrium state results in the following wetting boundary condition at the wall

$$\mathbf{n}_s \cdot \nabla c = \frac{\sqrt{2}}{2} \frac{\cos\theta_e}{\varepsilon}(1 - c^2), \tag{8}$$

where $\mathbf{n}_s$ denotes the outward normal to the solid surface. Despite boundary condition (8), the actual (apparent) contact angle θ of a moving contact line may actually differ in the course of the phase-field simulation from the equilibrium value θ_e depending on conditions (Yue and Feng, 2011; Wörner et al., 2021). On the inlet and outlet of the computational domain zero gradient boundary conditions are specified as

$$\mathbf{n}_f \cdot \nabla c = 0, \quad \mathbf{n}_f \cdot \nabla \phi_{\text{mix}} = 0, \tag{9}$$

where $\mathbf{n}_f$ denotes the outward normal at fluid boundaries.

The Cahn-Hilliard equation is used as evolution equation to minimise the free energy and is given by Jacqmin (1999) based on Cahn and Hilliard (1959)

$$\partial_t c + (\mathbf{u} \cdot \nabla) c = M \nabla^2 \phi_{\text{mix}}. \tag{10}$$

The second term on the left-hand side of equation (10) describes an advection term with velocity field $\mathbf{u}$ while the right-hand side represents a diffusive term with mobility parameter M. In the phase-field method, it is this diffusion term which enables contact line motion at a no-slip wall. As the mobility M constitutes the pre-factor of this term, its value directly affects the speed of the contact line. However, M represents no measurable physical quantity and should therefore be interpreted as a model parameter of the phase-field method.

To ensure compatibility of diffuse interface methods with the so-called sharp interface limit, the mobility is related to the capillary width. Following Jacqmin (1999), we here apply the scaling

$$M = \chi \varepsilon^2, \tag{11}$$

where χ is a constant. The value of this pre-factor will be determined in Section 3 by fitting numerical results obtained with different values of χ against classical approximate solutions for capillary imbibition in a straight planar gap. The capillary width is determined indirectly through definition of the Cahn number $Cn = \varepsilon / L_{\text{ref}}$, where L_{ref} is an appropriate characteristic macroscopic reference length chosen problem dependent, see below. In all present simulations, the Cahn number is set to $Cn = 0.02$.

2.2 Coupling with Navier-Stokes equations

To simulate the two-phase flow, the Cahn-Hilliard equation (10) is coupled with the Navier-Stokes equations.

Considering both phases as incompressible Newtonian fluids, the continuity equation becomes

$$\nabla \cdot \mathbf{u} = 0, \tag{12}$$

and the momentum equation is given by

$$\begin{aligned} &\partial_t(\rho_c \mathbf{u}) + \nabla \cdot (\rho_c \mathbf{u} \otimes \mathbf{u}) \\ &\quad = -\nabla \tilde{p} + \nabla \cdot [\mu_c(\nabla \mathbf{u} + (\nabla \mathbf{u})^\intercal)] + \mathbf{f}_g + \mathbf{f}_\sigma. \end{aligned} \tag{13}$$

The local values of density ρ_c and viscosity μ_c are calculated in dependence of the order parameter from the density/viscosity of the liquid (l) and gas (g) phases as follows

$$\begin{aligned} \rho_c &= \frac{1+c}{2}\rho_l + \frac{1-c}{2}\rho_g \text{ and} \\ \mu_c &= \frac{1+c}{2}\mu_l + \frac{1-c}{2}\mu_g. \end{aligned} \tag{14}$$

In the present study, the gap width (which is taken as L_{ref}) is always smaller than the capillary length scale, which is $\sqrt{\sigma/(\rho_l - \rho_g)|\mathbf{g}|} \approx 2.7$ mm for the considered air-water system. Gravitational forces are therefore neglected by setting $\mathbf{f}_g = \rho_c \mathbf{g} = 0$. According to Jacqmin (2000), the capillary force can be derived from the divergence of the well-known Korteweg stress tensor as

$$\mathbf{f}_\sigma = -c\nabla\phi, \tag{15}$$

leaving an additional gradient term which has been lumped into the pressure term, indicated by the tilde notation in (13).

2.3 Solution algorithms and numerical schemes

The above set of equations is discretised using the finite volume method in OpenFOAM (FOAM-extend 4.0) for unstructured meshes of general topology. We deploy the solver `phaseFieldFoam` which is an in-house code developed in cooperation between the Technical University of Darmstadt and the Karlsruhe Institute of Technology (Cai et al., 2015). It implements both segregated and coupled algorithms for the numerical solution of the coupled Navier-Stokes Cahn-Hilliard equations. Here, we choose the coupled algorithm. For the coupling of velocity and pressure the PIMPLE-algorithm in OpenFOAM was used with two outer correctors. For a description, the interested reader is referred to Holzmann (2019) and Greenshields and Weller (2022).

The main differences to the common algebraic volume-of-fluid method in the `interFoam` solver are briefly discussed next. For a detailed description of this code the reader is referred to Deshpande et al. (2012), see also Jamshidi et al. (2019) and Antritter et al. (2020). Phases are distinguished by the liquid volume fraction (α), which is in contrast to the order parameter in the range $0 \leq \alpha \leq 1$. Instead of the Cahn-Hilliard equation, the temporal evolution of the phase distribution is obtained by solution of a transport equation for α, where a counter-diffusion term serves to limit smearing of the conceptually sharp interface to about three mesh cells. In contrast to the free energy concept, surface tension is modelled as volume force by means of the continuum surface force model (Brackbill et al., 1992).

For the discretisation in time a first-order Euler scheme was used in both methods. For computational efficiency, we employ adaptive time-stepping. To determine the time step Δt, a Courant criterion with a value of $Co = |\mathbf{u}|_{\max}\Delta t/h = 0.1$ is applied in combination with an upper limit for the time step size ($\Delta t_{\max} = 1\,\mu$s). Here, h is the size of the uniform grid and $|\mathbf{u}|_{\max}$ the magnitude of the maximum velocity within the simulation domain.

For the discretisation in time a first-order Euler scheme was used. In space, second order Gauß schemes have been used. In the phase-field simulations, the limitedLinearV scheme for the convection term was used in the momentum equation and the Gamma scheme for the advection term in the Cahn-Hilliard equation. In the VOF simulations, the upwind scheme was used for convection in the momentum equation. In the transport equation for α, the vanLeer scheme for the advection term and a linear scheme for the counter-diffusion term were used. For the diffusion terms a linear scheme has been employed in both methods.

3 Capillary imbibition in straight channels

The motion of a liquid rising in a straight capillary channel is mathematically often approximated by ordinary differential equations of different forms allowing for analytical solution (Gonzáles-Santander and Martin, 2015; Berthier et al. 2015; Gründing, 2020). In numerical simulations with the phase-field method, the meniscus speed depends on the mobility parameter. In this Section, we use the mobility parameter as a fitting parameter, i.e., we try to find values for mobility pre-factor χ so that the meniscus speed is approximately the same as in the analytical solution for a given value of the contact angle.

3.1 Analytical solutions

The classical analytical approximation of capillary imbibition in a circular tube is the Lucas-Washburn law (Lucas, 1918; Washburn, 1921) which reads

$$x(t) = \left(\frac{R\sigma\cos\theta_e}{2\mu_l}\right)^{0.5} t^{0.5}. \tag{16}$$

Here, $x(t)$ denotes the distance of liquid penetration in the tube of radius R at time t. The derivation of the Lucas-Washburn equation takes into account capillary and viscous forces but neglects gravity and inertia.

For small penetration depths, the gravitational force is negligible, but inertial forces may have a notable influence. The analytical solution by Bosanquet (1923) takes liquid inertia into account and is given by

$$x(t) = \sqrt{\frac{2b}{a}t - \frac{2b}{a^2}\left(1 - e^{-at}\right)}. \tag{17}$$

The parameters a and b depend on physical properties and on the cross-sectional shape of the channel. For a circular pipe it is

$$a = \frac{8\mu_l}{\rho_l R^2} \quad \text{and} \quad b = \frac{2\sigma\cos\theta_e}{\rho_l R}. \tag{18}$$

For an infinite planar gap, the two terms a and b result in

$$a = \frac{12\mu_l}{\rho_l D^2} \quad \text{and} \quad b = \frac{2\sigma\cos\theta_e}{\rho_l D}, \tag{19}$$

where D is the distance between the parallel plates (Ouali et al., 2013).

The difference between equations (16) and (17) is visualised in Figure 3 for a case with $R = 0.5$ mm, $\theta_e = 45°$, $\rho_l = 998$ kg m^{-3}, $\mu_l = 0.001$ Pa s and $\sigma = 0.072$ N m^{-1}. Due to the strong influence of inertia for small time scales, the Bosanquet equation is used for determining the mobility parameter thereafter. Recently, Hua et al. (2021) published a combined analytical and experimental investigation of capillary imbibition in circular, square and rectangular channels, with dimensions that are in the same order of magnitude as the gaps investigated here. The results show a good agreement between the experiments and the Bosanquet equation, especially in the early stage of imbibition, which is relevant for our case.

Figure 3 Penetration depth of the meniscus for a capillary with radius $R = 0.5$ mm and contact angle $\theta_e = 45°$ according to Lucas-Washburn [equation (16)] and Bosanquet [equation (17)]

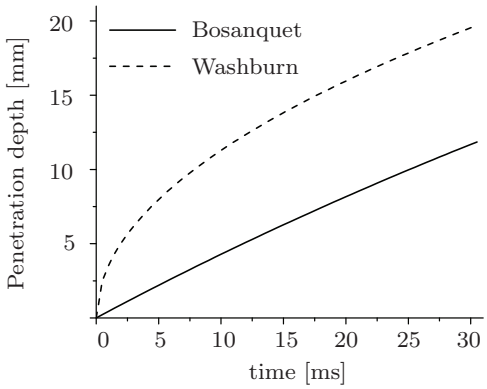

3.2 *Simulation setup for parallel plates*

The considered geometry is a gap formed by two parallel plates separated by a distance of $D = L_{\text{ref}} = 1$ mm [Figure 4(a)]. Due to symmetry, only half of the channel is simulated in combination with a symmetry boundary condition. The computational domain is meshed with a regular Cartesian grid consisting of square cells [Figure 4(b)]. With $Cn = 0.02$, the capillary width is given by $\varepsilon = 20$ µm resulting in a thickness of the diffuse interface region of $L_{\text{di}} = 83.28$ µm at equilibrium. In Cai et al. (2015), good agreement between numerical results and analytical solutions for various wetting phenomena is achieved if L_{di} is resolved by at least four cells, corresponding to $h = \varepsilon$. Based on this finding, a resolution of six cells corresponding to $h = 0.67\varepsilon$ is chosen here for all simulations. For the parallel plates setup, this leads to a mesh consisting of 36 cells along the width $D/2 = 0.5$ mm of the computational domain.

Figure 4 Validation set-up of water penetrating a gap between two parallel plates separated by distance D, (a) schematic 2D-geometry (b) mesh (c) initialisation of the order parameter (see online version for colours)

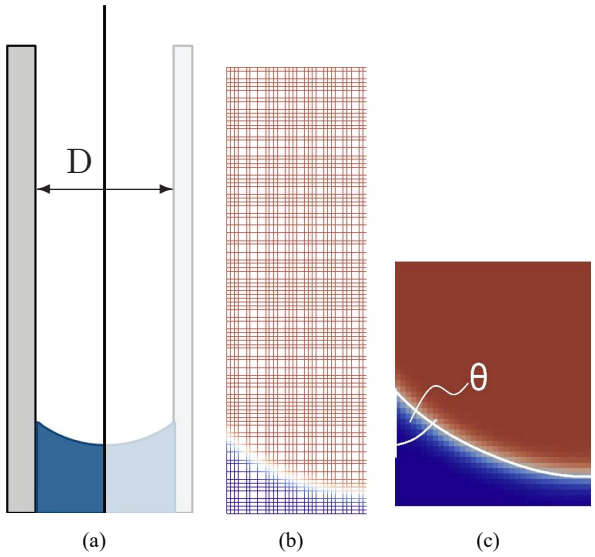

The meniscus is initialised as a circular segment so that the contact angle boundary condition at the wall is satisfied in combination with a horizontal profile at the symmetry boundary condition [Figure 4(c)]. Normal to the interface, c is initialised according to the equilibrium profile of the order parameter [equation (4)]. This initialisation reduces the oscillation of the meniscus in the beginning of the simulation. Further boundary conditions are given in Table 1. The boundary condition 'fixedFluxPressure' is a condition by OpenFOAM that adjusts the pressure gradient to meet the velocity boundary condition. For the third dimension, the boundary condition 'empty' is used in all simulations of this work to define a two dimensional setup in OpenFOAM.

Table 1 Boundary conditions used in present simulations

Parameter	*Wall*	*In-/outlet*
Order parameter c	fixed contact angle [equation (8)]	zero normal gradient
Velocity field **u**	no slip condition	zero normal gradient
Pressure p	fixedFluxPressure	zero total pressure
Chemical potential ϕ	zero normal gradient	zero normal gradient

Figure 5 Penetration depth for imbibition between parallel plates over time for equilibrium contact angle, (a) 45° (b) 85°

(see online version for colours)

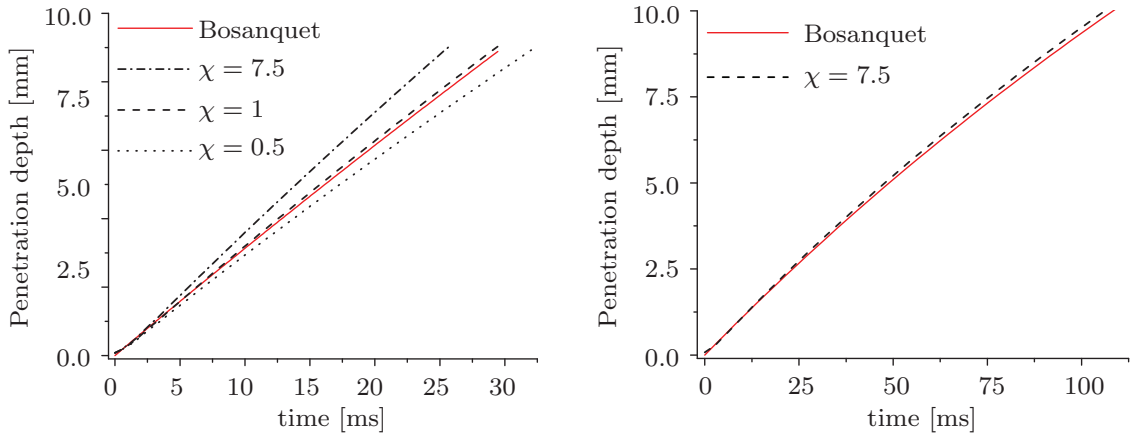

Note: Values of χ are in $\mathrm{m \cdot s \cdot kg^{-1}}$

Physical properties of air and water are taken at a temperature of 20°C as listed in Table 2. Two different equilibrium contact angles namely $\theta_e = 45^\circ$ and $\theta_e = 85^\circ$ were investigated with the parallel plates setup. The contact angle 85° is only slightly lower than the neutral contact angle, as for $\theta_e \geq 90^\circ$ no imbibition occurs.

Table 2 Physical properties

Property	*Unit*	*Water*	*Air*
Density ρ	$\mathrm{kg.m^{-3}}$	998	1.2
Dynamic viscosity μ	Pa.s	0.001	18.1×10^{-6}
Surface tension σ	$\mathrm{N.m^{-1}}$		0.072

For model calibration, a parameter study with respect to the mobility was carried out by variation of pre-factor χ [cf. equation (11)]. The penetration depth of water over time is displayed in Figure 5 and compared to the analytical approach by Bosanquet. In Figure 5(a), the penetration depth is plotted for simulations with three different values of χ (7.5, 1, 0.5 $\mathrm{m \cdot s \cdot kg^{-1}}$). It can be seen that the penetration speed is higher for larger values of χ corresponding to larger values of the mobility. Considering that the diffusive term of the Cahn-Hilliard equation, which enables the contact line motion, is proportional to χ, this is to be expected. A similar dependence of imbibition speed on mobility in phase-field simulations has been reported by Xiao et al. (2019).

For the contact angle $\theta_e = 45^\circ$ a value of $\chi = 1$ $\mathrm{m \cdot s \cdot kg^{-1}}$ leads to a good agreement with the analytical solution, whereas for $\theta_e = 85^\circ$ a value of $\chi = 7.5$ $\mathrm{m \cdot s \cdot kg^{-1}}$ gives good agreement. Notably, the value of χ that gives best agreement depends on the contact angle. The values for χ determined here will be used in the next Section to study the capillary imbibition in a generalised sealing gap geometry. It should be noted that the value of χ that gives best agreement with Bosanquet theory may depend on further parameters such as the gap width D (Hagg, 2019), which is however no varied here.

4 Capillary imbibition in a generalised sealing gap geometry

In this Section, the imbibition of water in a sealing gap with a pinning groove is studied in absence of gravity. The purpose of the groove is to prevent water from reaching the sealing ring by utilising the pinning effect that occurs at the sharp edge. It thus creates an obstacle for the further advancement of the contact line. At such a pinned meniscus, evaporation may occur in reality which is, however, not considered in the present simulations. It has been shown that evaporation enhances pinning of contact lines at sharp edges, even for the case of perfectly wetting liquids (Tsoumpas et al., 2014).

4.1 Geometry and numerical set-up

The geometry of the generalised planar sealing gap is schematically shown in Figure 6(a). The right-angled corner of the pinning groove corresponds to an angle $\alpha = 90^\circ$ for the present acute edge. Figure 6(b) shows the two-dimensional computational domain with the initialisation of the order parameter. A rectangular area is initialised as water reservoir, representing a part of the droplet shown in Figure 1. In the real 3D geometry, incoming water will displace the air. In the simplified planar geometry displayed in Figure 6(a), the air cannot flow out of the domain and water would thus not penetrate the gap. To allow the escape of air, a thin outlet is added on the right side of the computational domain, see Figure 6(b). The top, left and bottom boundaries of the part of the computational domain that is initialised with water and the right boundary of the thin additional outlet are defined as 'in-/outlet'. All other boundaries are defined as 'wall' (cf. Table 1). In the third dimension, the boundary condition 'empty' for a two-dimensional setup is used. At the beginning of the simulation, both phases are at rest and the meniscus is straight.

Figure 6 Planar sealing gap setup with measurements, (a) sketch with generalised dimensions (b) computational domain with initial phase distribution [blue = water ($c_l = 1$), red = air ($c_g = -1$)] (see online version for colours)

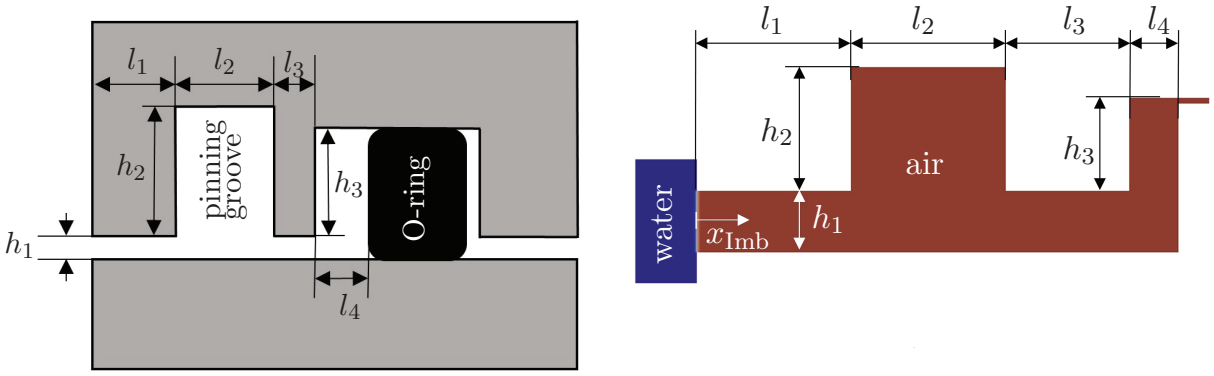

(a) (b)

Note: The pinning groove has width l_2 and height h_2.

The dimensions of the specific simulation case are listed in Table 3. In the phase-field simulations, the capillary width (ε) is the same as for the parallel plates setup with $Cn = 0.02$ and $L_{\mathrm{ref}} = h_1 = 1$ mm. The size of the square mesh cells is therefore the same as in Section 3.2, which leads to $83,268$ cells for the whole computational domain. For the simulation with $\theta_e = 45°$ the time step criterion was reduced from $Co = 0.1$ to $Co = 0.05$ after $t = 36$ ms. The same mesh and a corresponding set-up is also used for the VOF simulations in combination with $Co = 0.1$.

Table 3 Dimensions of investigated sealing gap (in mm), cf. Figure 6

h_1	h_2	h_3	l_1	l_2	l_3	l_4
1	2	1.5	2.5	2.5	2	0.8

4.2 Results

Simulations are first performed for equilibrium contact angles $\theta_e = 45°$ and $\theta_e = 85°$ which can be considered as typical for water in contact with housing materials. The opening angle of the solid edge that is relevant for the pinning effect is a right angle so that $\alpha = 90°$. For the housing material with $\theta_e = 45°$, the interface is therefore expected to be in the pinned state as long the actual contact angle at the edge is in the range $45°$–$135°$. For a housing material with $\theta_e = 85°$ instead, pinning occurs as long the actual contact angle is in the range $85° - 175°$. Results obtained with the phase-field method for these two contact angles are discussed in detail and thereafter compared with results obtained by the VOF method. Finally, results of phase-field simulations for four further values of the contact angle are presented to study the influence of wettability in more detail.

4.2.1 *Time evolution of water penetration for contact angle $\theta_e = 45°$*

In the phase-field simulation for contact angle $\theta_e = 45°$, the mobility pre-factor is chosen as $\chi = 1\ \mathrm{m \cdot s \cdot kg^{-1}}$ according to Section 3. The progress of water penetrating into the sealing geometry is shown in Figure 7(a)–7(h) for selected instants in time.

In the beginning, the capillary force in the middle of the meniscus is very small due to the flat initialisation of the interface. In contrast, the capillary force at the wall is high as the initial contact angle differs from the equilibrium value. This mismatch results in a high penetration speed close to the walls. Accordingly, a water flow from the middle of the meniscus towards the walls occurs which leads to a withdrawal of the water in the middle of the meniscus during the first millisecond [Figure 7(a)].

The large penetration speed differences between the meniscus at the wall and the meniscus in the middle result in a strong curvature and in strong capillary forces in the middle of the meniscus. This leads to higher penetration speeds in the middle of the meniscus which result in an almost flat meniscus again [Figure 7(b)] and a deviation of the apparent contact angle from the equilibrium contact angle prescribed by boundary condition (8). This oscillation between large and small meniscus curvature in the mid-plane of the gap becomes smaller over time and a constant penetration speed over the whole meniscus is reached after a few milliseconds. In Figure 8, the penetration depth in the middle of the meniscus is plotted over time to visualise the oscillation, a phenomenon known as entrance effect. Classical one-dimensional approximations do not account for changes of the meniscus shape. Accordingly, the Bosanquet curves in Figures 5 and 8 exhibits no oscillations corresponding to the entrance effect. In Figure 8, furthermore the slopes of the two curves differ. In Bosanquet theory the penetration speed is larger as compared to the simulation because the additional inertia of the stagnant water initialised in front of the sealing gap geometry is not taken into account.

Figure 7 Penetration of water (blue) into the sealing gap for $\theta_e = 45^\circ$, (a) $t = 0.8$ ms (b) $t = 2.0$ ms (c) $t = 11.2$ ms (d) $t = 15.2$ ms (e) $t = 82.8$ ms (f) $t = 100.8$ ms (g) $t = 111.6$ ms (h) $t = 121.6$ ms (see online version for colours)

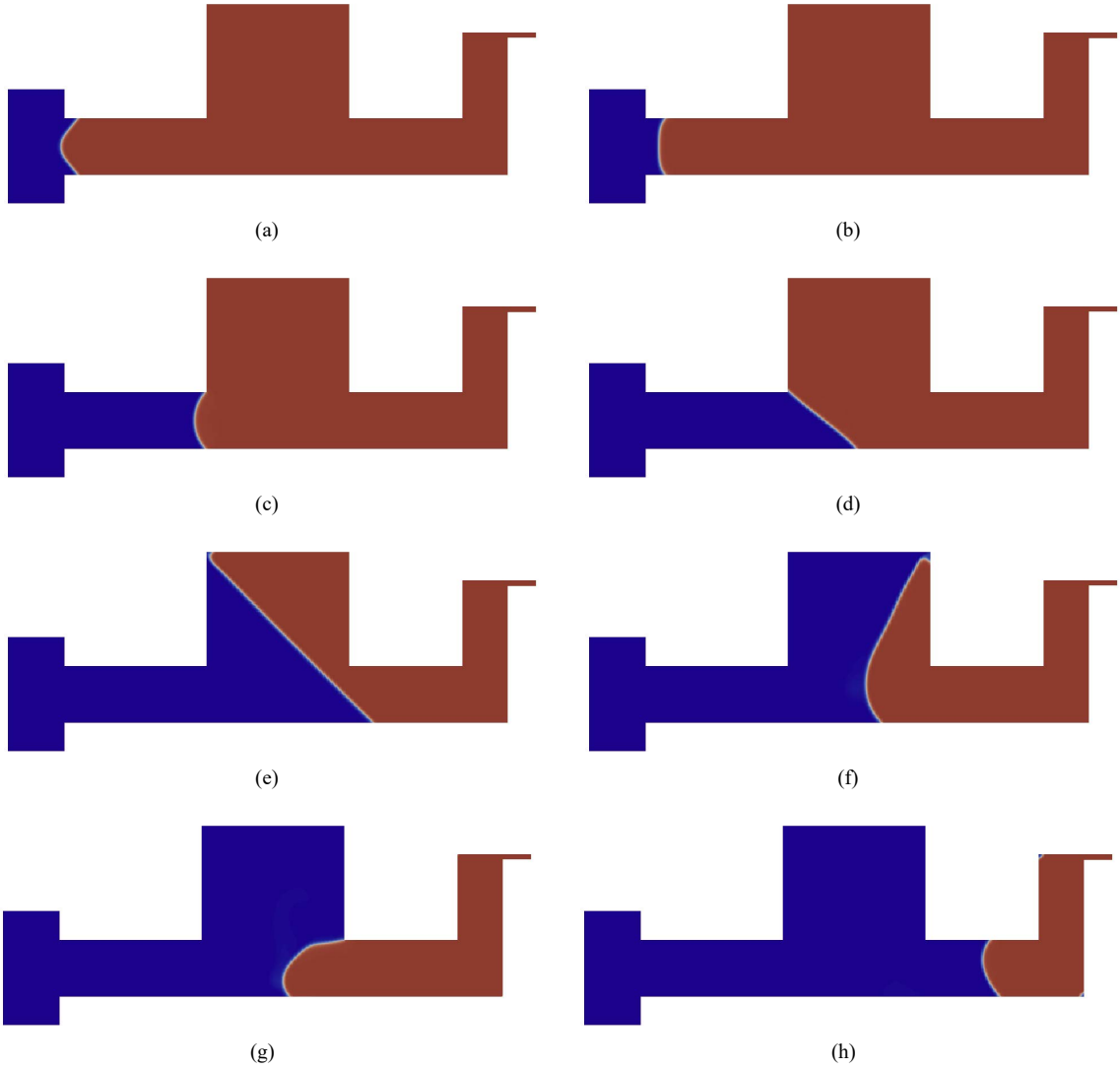

Figure 8 Penetration depth in the middle of meniscus for $\theta_e = 45^\circ$ to visualise the oscillation associated with the entrance effect at the beginning of the simulation

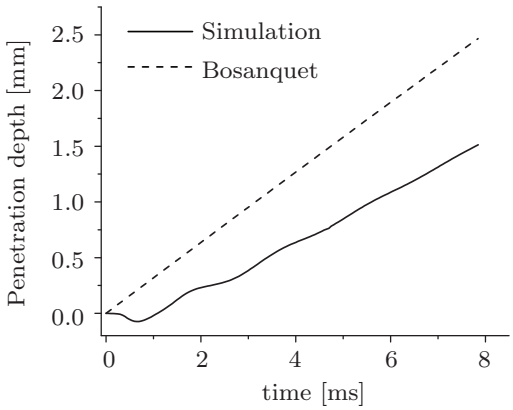

When the upper contact line reaches the edge of the pinning groove at $t = 11.2$ ms, the meniscus has a round shape [Figure 7(c)]. At this instant in time, the actual contact angle at the edge is equal to the equilibrium contact angle. From $t = 11.2$ ms to $t = 15.2$ ms, the top contact line is pinned at the edge. Meanwhile the bottom contact line continues to penetrate the gap until a straight meniscus is reached, where the lower contact angle equals the equilibrium values of 45° while the contact angle at the edge is 135°. The latter value corresponds to the critical contact angle θ_{cr} where contact lining pinning is possible. Due to liquid inertia, the contact angle at the lower wall becomes slightly lower than 45° at $t = 15.2$ ms [Figure 7(d)]. Accordingly, the contact angle at the edge exceeds the limiting angle of 135° and the contact line moves around the edge. Thereafter water penetrates with a straight meniscus into the sealing gap while the upper contact angle moves along the vertical wall of the pinning groove.

At $t = 82.2$ ms, the upper contact line reaches the top wall of the pinning groove and rapidly adjusts to the contact angle boundary condition [Figure 7(e)]. This leads to a fast movement of the meniscus at the top and strong deformations of the meniscus shape. These deformations lead to a withdrawal at the bottom of the sealing gap, which can be seen at $t = 100.8$ ms when the top contact line reaches the right wall of the pinning groove [Figure 7(f)]. At $t = 111.6$ ms, a second pinning of the top three-phase contact line can be observed [Figure 7(g)].

At the last displayed instant in time ($t = 121.6$ ms) the water got past the pinning groove and entered the gap toward the sealing ring. The comparison with Figure 7(g) suggests, that the lower contact line moves with faster speed as compared to the upper contact line which results in different apparent contact angles at both walls. At this late stage of the simulation, numerical artefacts appear as seen in the bottom right and the top left corner of the remaining gas area [Figure 7(h)]. The origin of these artefacts is related to small errors in the boundedness of the order parameter which stays not in the physical plausible limits $-1 \leq c \leq 1$. These errors in boundedness interfere with the boundary condition (8) in the corners of the computational domain and accumulate over time. Note that equation (8) presumes $c^2 \leq 1$ which is not guaranteed in the numerical solution here. For the present study, these artefacts do not affect the conclusions regarding meniscus behaviour at the pinning groove. Nevertheless, it is important to improve the implementation to avoid such artefacts in future computations.

4.2.2 *Time evolution of water penetration for contact angle $\theta_e = 85°$*

A similar phase-field simulation was performed for the higher contact angle of $85°$ using $\chi = 7.5\,\mathrm{m \cdot s \cdot kg^{-1}}$ according to Section 3. Figure 9 shows the instantaneous order parameter distribution for two different instants in time. At the moment of deepest water imbibition ($t = 50$ ms), the meniscus has a convex shape [Figure 9(a)]. At this instant in time the water contact angle with the horizontal surface of the upper housing part is about $122°$ which is sufficiently far from the critical angle $\theta_{\mathrm{cr}} = 175°$ relevant for pinning by the edge effect. After $t = 50$ ms the penetration depth of the bottom contact line decreases again and thereafter oscillates around a mean value as shown in Figure 10 to be discussed below. The upper contact line stays pinned at the edge of the pinning groove from time $t = 50$ ms till the end of the simulation. At $t = 180$ ms a steady state is reached with a flat meniscus according to the prescribed equilibrium contact angle $\theta_e = 85°$ with the bottom wall [Figure 9(b)]. Remarkably, no numerical corner artefacts are observed for this simulation despite the larger problem time. The reason may be that the wetting boundary condition (8) depends on $\cos\theta_e$ with the right-hand-side approaching zero for $\theta_e \to 90°$. Figure 9(c) shows the velocity magnitude at the end of the simulation. While both phases are at rest, a maximum velocity of 0.15 m/s occurs at the two static contact lines corresponding to parasitic currents.

Figure 9 Penetration of water (blue) into the sealing gap for $\theta_e = 85°$ for two different instants in time and velocity magnitude at steady state, (a) deepest penetration at bottom wall ($t = 50$ ms) (b) steady state ($t = 180$ ms) (c) velocity magnitude (m/s) at steady state ($t = 180$ ms) (see online version for colours)

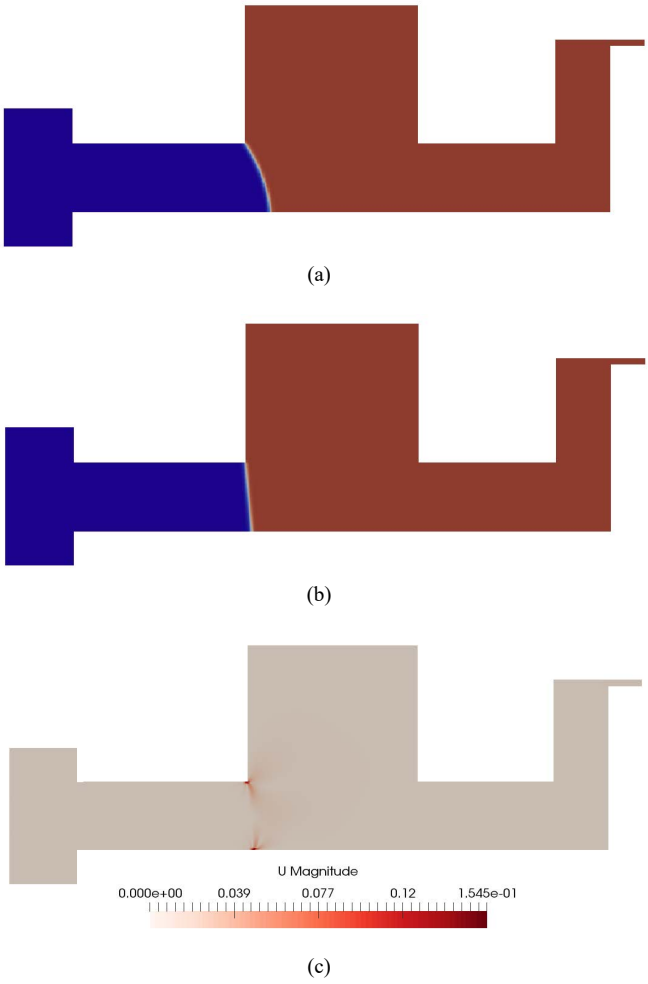

Summing up, in the case with $\theta_e = 85°$ imbibition is stopped by the pinning groove and water is prevented from reaching the sealing ring. This pinning effect is of high practical interest when designing sealing geometries because it can prevent corrosion and infiltration at the contact surface between the sealing ring and the metal housing.

4.2.3 *Comparison with VOF computations and influence of housing wettability*

For a quantitative comparison of simulations with different contact angle, we display in Figure 10 the penetration depth of the three-phase contact line at the bottom wall over time. In contrast to the case with $\theta_e = 45°$, no notable oscillation of the meniscus position at the beginning of the simulation

associated with the entrance effect is observed for $\theta_e = 85°$. The different behaviour can be explained by the initial conditions given by a flat meniscus with apparent contact angle $\theta_0 = 90°$. For $\theta_e = 45°$, the difference from θ_0 is large, therefore the significant entrance effect. For $\theta_e = 85°$ the difference from θ_0 is instead very small resulting only in a small initial mismatch of the contact angle. Accordingly, the bottom contact line and the entire meniscus penetrate the sealing gap with almost constant speed until $t \approx 50$ ms, where the penetration depth of the bottom contact line reaches a maximum. Thereafter, the position of the lower contact line oscillates with decreasing amplitude around a mean position before coming to rest. Qualitatively, these oscillations are similar to those reported for capillary rise in a short tube where the meniscus is finally pinned at the edge of the tube (Xiao et al., 2020).

Figure 10 Meniscus position at the bottom wall of the sealing gap geometry for different contact angles in phase-field and VOF method (see online version for colours)

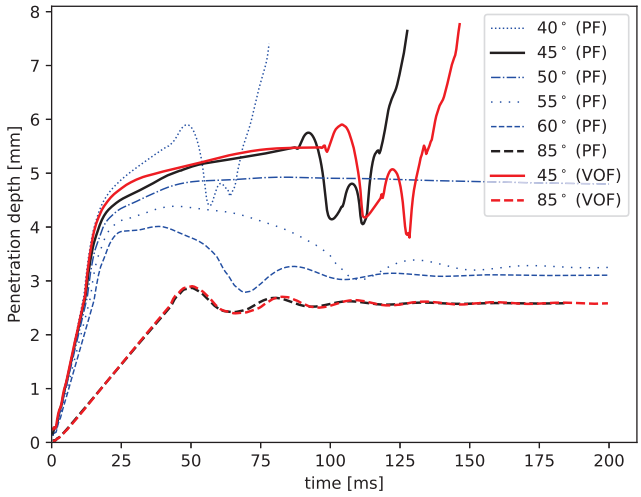

Similar simulations for contact angles $\theta_e = 45°$ and $\theta_e = 85°$ were performed with the VOF method using `interFoam`. Figure 10 shows that the time evolution of the bottom contact line penetration depth is quite similar for both methods. For $\theta_e = 85°$, permanent pinning of the upper contact line at the edge is observed for the VOF method as well and the terminal location of the meniscus is virtually identical with both methods. Similar to Figure 9(c), the maximum spurious currents at the end of the simulation occur in the vicinity of the two static contact lines, but are a factor 20 higher compared to the phase-field method. This observation is in agreement with the results reported by Jamshidi et al. (2019) and Antritter et al. (2020). On the other hand, no errors of the phase distribution in domain corners is observed for the VOF method in contrast to the phase-field simulations.

To study the effect of the housing material wettability on the efficiency of the pinning groove, further simulations were performed with the phase-field method for contact angles $40°$, $50°$, $55°$ and $60°$. For all contact angles, the mobility value determined for the case with $45°$ is used. The corresponding results for the bottom contact line penetration depth are displayed as thin blue lines in Figure 10. The curve for $\theta_e = 40°$ is qualitative similar to that for $\theta_e = 45°$ while penetration speed is higher and filling of the pinning groove occurs faster. For $\theta_e = 50°$, the meniscus moves around the pinning edge and stops before reaching the upper left corner of the pinning groove. The almost flat meniscus then recedes with very low velocity. For contact angles $55°$ and $60°$, the upper contact line moves around the pinning edge as well but recedes with larger velocity as compared to the case with $50°$. Finally, the flat meniscus is pinned at the edge with the penetration depth of the bottom contact line corresponding to the respective contact angle. Our study thus suggests that due to liquid inertia, the minimum housing material contact angle for achieving water stop at the edge of the pinning groove is not $45°$ as predicted by the Gibbs criterion but rather $55°$.

5 Concluding discussion

In this work, a phase-field model based on the coupled Cahn-Hilliard Navier-Stokes equations is used to study capillary-driven penetration into a generalised sealing gap geometry. In order to ensure physically plausible penetration speeds, the influence of the mobility parameter on the imbibition of water into a gap between two parallel plates was investigated for two different contact angles. For two representative contact angles, an appropriate value of the mobility was determined by comparing simulation results with the analytical Bosanquet equation. Based on the determined mobility values, the penetration of water into a geometrically complex planar sealing gap with pinning groove was simulated for six different contact angles of the housing material. The pinning groove slowed down the imbibition process for contact angles up to about $50°$, but did not stop penetration. Instead for contact angles larger than about $55°$ water penetration towards the sealing ring is prevented due to contact line pinning. Volume-of-Fluid simulations for two contact angles performed for comparison, show similar behaviour with slight differences in imbibition speed and much larger spurious currents. The striking influence of the contact angle on the completely different imbibition outcome is explained by the edge effect. It can be concluded that for the considered sealing gap geometry, a stop of water imbibition by the edge effect is only possible for housing materials with contact angles larger than about $55°$.

Overall, the phase-field method appears as a powerful tool to study capillary-driven imbibition in complex geometries and is able to model pinning effects at acute edges without further adjustments. A certain disadvantage is, however, that the mobility which notably affects the speed of the three-phase contact line is no measurable physical quantity. Thus, a prior calibration of this model parameter is recommended. Different values of the mobility may result in different imbibition speeds. However, larger imbibition speeds may in general not affect the ultimate

simulation outcome, i.e., whether permanent pinning occurs or not, at least as long as liquid inertia is not predominant. A practical conservative guideline may thus be to perform a sensitivity study with large values of the mobility to ensure the physical plausibility of simulation results concerning contact line pinning by the edge effect.

The present simulations demonstrate the complex influence of the sealing gap shape and surface wettability on water propagation in the sealing gap towards the seal. Hence, those factors can also be considered in design of enclosures in addition to the sealing layout, material selection and surface treatment. In order to perform engineering design optimisations or endurance tests for practical applications, further influences such as gravitational force, pressure or contact angle changes due to ageing of the surface have to be taken into account in combination with full 3D simulations. Furthermore, to ensure the reliability of the simulations, comparisons with experiments have to be conducted.

Acknowledgements

H.M. thanks for funding of this work by the Deutsche Forschungsgemeinschaft (DFG, German Research Foundation) Project-ID 265191195 SFB 1194.

References

Antritter, T., Mayer, M., Hachmann, P. and Wörner, M. (2020) 'Suppressing artificial equilibrium states caused by spurious currents in droplet spreading simulations with dynamic contact angle model', *Progress in Computational Fluid Dynamics*, Vol. 20, No. 2, pp.59–70, DOI: 10.1504/PCFD.2020.106403.

Berthier, J., Gosselin, D. and Berthier, E. (2015) 'A generalization of the Lucas-Washburn-Rideal law to composite microchannels of arbitrary cross section', *Microfluid Nanofluid*, Vol. 19, pp.497–507, DOI: 10.1007/s10404-014-1519-3.

Bosanquet, C. (1923) 'On the flow of liquids into capillary tubes', *The London, Edinburgh, and Dublin Philosophical Magazine and Journal of Science*, Vol. 45, No. 267, pp.525–531, DOI: 10.1080/14786442308634144.

Börnhorst, M., Cai, X., Wörner, M. and Deutschmann, O. (2019) 'Maximum spreading of urea water solution during drop impingement', *Chemical Engineering Technology*, Vol. 42, No. 11, pp.2419–2427, DOI: 10.1002/ceat.201800755.

Brackbill, J.U., Kothe, D.B. and Zemach, C. (1992) 'A continuum method for modeling surface tension', , *Journal of Computational Physics*, Vol. 100, No. 2, pp.335–354, DOI: 10.1016/0021-9991(92)90240-y.

Bray, A.J. (1994) 'Theory of phase-ordering kinetics', *Advances in Physics*, Vol. 43, pp.357–459, DOI: 10.1080/00018739400101505.

Cahn, J.W. and Hilliard, J.E. (1958) 'Free energy of a nonuniform system. I. Interfacial free energy', *Journal of Chemical Physics*, Vol. 28, No. 2, pp.258–267.

Cahn, J.W. and Hilliard, J.E. (1959) 'Free energy of a nonuniform system. III. Nucleation in a two-component incompressible fluid', *Journal of Chemical Physics*, Vol. 31, No. 3, pp.688–699.

Cai, X., Marschall, H., Wörner, M. and Deutschmann, O. (2015) 'Numerical Simulation of Wetting Phenomena with a Phase-Field Method using OpenFOAM', *Chemical Engineering & Technology*, Vol. 38, No. 11, pp.1985–1992.

Deshpande, S.S., Anumolu, L. and Trujillo, M.F. (2012) 'Evaluating the performance of the two-phase flow solver interFoam', *Computational Science & Discovery*, Vol. 5, No. 1, p.014016, DOI: 10.1088/1749-4699/5/1/014016.

Dyson, D.C. (1988) 'Contact line stability at edges: comments on Gibbs's inequalities', *The Physics of Fluids*, Vol. 31, pp.229–232, DOI: 10.1063/1.866851.

Fink, V., Cai, X., Stroh, A., Bernard, R., Kriegseis, J., Frohnapfel, B., Marschall, H. and Wörner, M. (2018) 'Drop bouncing by micro-grooves', *International Journal of Heat and Fluid Flow*, Vol. 70, pp.271–278.

Gibbs, J.W. (1961) *The Scientific Papers: Vol. 1*, p.326, Dover Publications, New York.

Ginzburg, V.L. and Landau, L.D. (1950) 'On the theory of superconductivity', *Zh. Eksp. Teor. Fiz.*, Vol. 20, pp.1064–1082.

Gonzáles-Santander, J.L. and Martin, G. (2015) 'New analytical approximations for the liquid rise in a capillary tube', *Fluid Dynamics Research*, Vol. 47, p.025505, DOI: 10.1088/0169-5983/47/2/025505.

Gosselin, D., Berthier, J., Chaussy, D. and Belgacem, N. (2015) 'Capillary flows: dynamics and geometry effects', *Proceedings of the 2015 COMSOL Conference in Grenoble*, DOI: 10.1016/j.cpc.2018.10.015.

Greenshields, C. and Weller, H. (2022) *Notes on Computational Fluid Dynamics: General Principles*, CFD Direct Ltd, Reading, UK.

Grishaev, V., Amirfazli, A., Chikov, S., Lyulin, Y. and Kabov, O. (2013) 'Study of edge effect to stop liquid spillage for microgravity application', *Microgravity Sci. Technol.*, Vol. 25, pp.27–33, DOI: 10.1007/s12217-012-9325-6.

Gründing, D. (2020) 'An enhanced model for the capillary rise problem', *International Journal of Multiphase Flow*, Vol. 128, p.103210, DOI: 10.1016/j.apm.2020.04.020.

Gründing, D., Smuda, M., Antritter, T., Fricke, M., Rettenmaier, D., Kummer, F., Stephan, P., Marschall, H. and Bothe, D. (2020) 'A comparative study of transient capillary rise using direct numerical simulations', *Applied Mathematical Modelling*, Vol. 86, pp.142–165, DOI: 10.1016/j.apm.2020.04.020.

Hagg, D. (2019) *Direkte numerische Simulation von transientem Benetzungsverhalten in komplexen Dichtspaltgeometrien unter Verwendung von phaseFieldFoam*, Master's thesis, Karlsruhe Institute of Technology, KITopen, DOI: 10.5445/IR/1000145948.

He, Q. and Kasagi, N. (2008) 'Phase-field simulation of small capillary-number two-phase flow in a microtube', *Fluid Dynamics Research*, Vol. 40, Noa. 7–8, p.497, DOI: 10.1002/ceat.201800755.

Holzmann, T. (2019) '*Mathematics, Numerics, Derivations and OpenFOAM*, Holzmann CFD, Release 7.0 [online] https://holzmann-cfd.de (accessed 7 February 2023).

Hua, W., Zhou, W., Wang, W., Wang, Z., Wu, R. and Zhu, L. (2021) 'Maximization of the capillary pump efficiency in microfluidics', *SN Applied Sciences*, Vol. 315, No. 3, pp.2523–3971, DOI: 10.1007/s42452-021-04293-1.

Jacqmin, D. (1999) 'Calculation of two-phase Navier-Stokes flows using phase-field modeling', *Journal of Computational Physics*, Vol. 155, No. 1, pp.96–127.

Jacqmin, D. (2000) 'Contact-line dynamics of a diffuse fluid interface', *Journal of Fluid Mechanics*, Vol. 402, pp.57–88.

Jamshidi, F., Heimel, H., Hasert, M., Cai, X., Deutschmann, O., Marschall, H. and Wörner, M. (2019) 'On suitability of phase-field and algebraic volume-of-fluid OpenFOAM solvers for gas liquid microfluidic applications', *Computer Physics Communications*, Vol. 236, pp.72–85, DOI: 10.1016/j.cpc.2018.10.015.

Lee, H.G., Yang, J. and Kim, J. (2020) 'Pinning boundary conditions for phase-field models', *Communications in Nonlinear Science and Numerical Simulation*, Vol. 82, p.105060, DOI: 10.1016/j.cnsns.2019.105060.

Lucas, R. (1918) 'Ueber das Zeitgesetz des kapillaren Aufstiegs von Flüssigkeiten', *Kolloid-Zeitschrift*, Vol. 23, pp.15–22, DOI: 10.1007/BF01461107.

Mehrabian, H., Gao, P. and Feng, J.J. (2011) 'Wicking flow through microchannels', *Physics of Fluids*, Vol. 23, No. 12, p.122108.

Mirjalili, S., Jain, S.S. and Dodd, M.S. (2017) 'Interface-capturing methods for two-phase flows: an overview and recent developments', *Center for Turbulence Research Annual Research Briefs*, pp.117–135.

Oliver, J.F., Huh, C. and Mason, S.G. (1977) 'Resistance to spreading of liquids by sharp edges', *Journal of Colloid and Interface Science*, Vol. 59, No. 3, pp.568–581, DOI: 10.1016/0021-9797(77)90052-2.

Ouali, F.F., McHale, G., Javed, H., Trabi, C., Shirtcliffe, N.J. and Newton, M.I. (2013) 'Wetting considerations in capillary rise and imbibition in closed square tubes and open rectangular cross-section channels', *Microfluidics and Nanofluidics*, Vol. 15, No. 3, pp.309–326, DOI: 10.1007/s10404-013-1145-5.

Peng, X., Wang, X., Du, Z. and Zeng, F. (2021) 'Phase-field simulations of precursor film in microcapillary imbibition for liquid-liquid systems', *International Journal of Multiphase Flow*, Vol. 144, p.103789, DOI: 10.1016/j.ijmultiphaseflow.2021.103789.

Samkhaniani, N., Stroh, A., Holzinger, M., Marschall, H., Frohnapfel, B. and Wörner, M. (2021) 'Bouncing drop impingement on heated hydrophobic surfaces', *International Journal of Heat and Mass Transfer*, Vol. 180, p.121777.

Tsoumpas, Y., Dehaeck, S., Galvagno, M., Rednikov, A., Ottevaere, H., Thiele, U. and Colinet, P. (2014) 'Nonequilibrium Gibbs' criterion for completely wetting volatile liquids', *Langmuir*, Vol. 30, No. 40, pp.11847–11852, DOI: 10.1021/la502708f.

Van der Waals, J.D. (1893) 'The thermodynamic theory of capillarity under the hypothesis of a continuous variation of density', *Verhandel. Konink. Akad. Weten. 1 (English) J. Stat. Phys.*, Vol. 20, No. 1979, DOI: 10.1007/BF01011514.

Washburn, E.W. (1921) 'The dynamics of capillary flow', *The Physical Review*, Vol. 17, No. 3, pp.273–283.

Wiklund, H. (2012) *Lattice Boltzmann Simulations of Two-Phase Flow in Fibre Network System*, Doctoral dissertation, Mid Sweden University, Diva Portal [online] https://www.diva-portal.org/smash/get/diva2:534255/FULLTEXT01.pdf (accessed 7 February 2023).

Wörner, M. (2012) 'Numerical modeling of multiphase flows in microfluidics and micro process engineering: a review of methods and applications', *Microfluidics and Nanofluidics*, Vol. 12, No. 6, pp.841–886, DOI: 10.1007/s10404-012-0940-8.

Wörner, M., Samkhaniani, N., Cai, X., Wu, Y., Majumdar, A., Marschall, H., Frohnapfel, B. and Deutschmann, O. (2021) 'Spreading and rebound dynamics of sub-millimetre urea-water-solution droplets impinging on substrates of varying wettability', *Applied Mathematical Modelling*, Vol. 95, pp.53–73, DOI: 10.1016/j.apm.2021.01.038.

Xiao, J., Luo, Y., Niu, M., Wang, Q., Wu, J., Liu, X. and Xu, J. (2019) 'Study of imbibition in various geometries using phase field method', *Capillarity*, Vol. 2, No. 4, pp.57–65.

Xiao, J., Liu, X., Luo, Y., Cai, J. and Xu, J. (2020) 'Oscillations of free surface at the edge of short capillary tubes', *Colloids and Surfaces A: Physicochemical and Engineering Aspects*, Vol. 591, p.124572.

Yue, P. and Feng, J.J. (2011) 'Can diffuse-interface models quantitatively describe moving contact lines?', *European Physical Journal: Special Topics*, Vol. 197, pp.37–46, DOI: 10.1140/epjst/e2011-01434-y.

Yue, P., Zhou, C. and Feng, J.J. (2010) 'Sharp-interface limit of the Cahn-Hilliard model for moving contact lines', *Journal of Fluid Mechanics*, Vol. 645, pp.279–294.

Zeng, D., Zhong, Y., Cao, D., Zhao, P., Fu, T. and Qi, Y. (2022) 'Corrosion damage behaviors of rubber O-rings under simulated acid fracturing conditions', *Petroleum*, in press, DOI: 10.1016/j.petlm.2021.05.001.

Zimmermann, M., Hunziker, P. and Delamarche, E. (2008) 'Valves for autonomous capillary systems', *Microfluid Nanofluid*, Vol. 5, pp.395–402, DOI: 10.1007/ s10404-007-0256-2.